Vertical Mass Flux Calculations in Hawaiian Trade Cumulus Clouds from Dual-Doppler Radar

SCOTT A. GRINNELL,* CHRISTOPHER S. BRETHERTON,[+] DAVID E. STEVENS,[#] AND ALISTAIR M. FRASER[+]

*Geophysics Program, University of Washington, Seattle, Washington
[+]Department of Atmospheric Sciences, University of Washington, Seattle, Washington
[#]Courant Institute of Mathematical Sciences, New York, New York

(Manuscript received 21 November 1994, in final form 9 January 1996)

ABSTRACT

Two ground-based Doppler radars and an instrumented aircraft provided a means for computing the vertical mass flux in trade wind cumulus clouds that formed east of the island of Hawaii during the Hawaiian Rainband Project of 1990. This study compares the mass fluxes of small isolated cells with larger groups of clouds and rainbands. Because of excellent sensitivity, the 5.5-cm wavelength radars were capable of detecting Bragg backscatter, which extended the measurements to include some precipitation-free air within and surrounding the clouds.

The shape of the vertical profile of vertical mass flux within shallow cumulus clouds and cloud groups varied considerably over the cloud's life cycle but was comparatively independent of cloud size. The early stages of convection displayed a mass flux profile that resembled those produced by buoyancy sorting and entraining plume models, but the mature and later stages were considerably more affected by precipitation-driven downdrafts and included mean downward mass fluxes. The vertical mass flux profiles predicted by a three-dimensional LES model of an isolated cumulus cloud showed the same evolutionary phases as the observations.

1. Introduction

Numerical modeling of weather and climate, particularly in the Tropics and subtropics, relies heavily on cumulus parameterization—the ability to parameterize accurately the vertical transport of heat, moisture, and momentum in both deep and boundary-layer cumulus cloud ensembles (e.g., Tiedtke et al. 1988). Most cumulus parameterizations are built around a conceptual model of a typical cumulus cloud that describes the transports by that cloud over its lifetime. Such conceptual models include the entraining plume model (Stommel 1947), buoyancy sorting models (Raymond and Blyth 1986; Emanuel 1991), and mixing line models (Betts 1985), often modified to account for downdrafts driven by precipitation. Conceptual models have been very difficult to test observationally, especially for shallow convection with its small length and time scales. Because of this, cumulus parameterizations are typically tested by examining their impact on forecasts or climatology, or occasionally by comparison with a few regional datasets such as the Barbados Oceanographic and Meteorological Experiment (BOMEX 1969) for. shallow clouds or the Global Atmospheric Research

Program's Atlantic Tropical Experiment (GATE 1974) for deep clouds. Large eddy simulations (Sommeria 1976; Siebesma and Cuijpers 1995) have become a useful tool for examining model assumptions for shallow cumuli but are not a substitute for observations.

A central feature of a conceptual model of a cumulus cloud is a model of the vertical mass transport within the cloud and the manner in which it varies with height due to entrainment of air into the cloud and detrainment of air out of the convective region. An entraining plume model, for instance, predicts increasing mass transport with height due to lateral entrainment, with all detrainment taking place at cloud top. In a buoyancy sorting model, entrainment and detrainment both take place at all heights within the cloud layer, so mass transport may actually decrease with height above cloud base. In parameterizations, such as those used by Arakawa and Schubert (1974), that postulate a spectrum of cloud types, the overall vertical mass transport depends strongly on the spectrum of cloud sizes. It has long been recognized that direct observations of the vertical profile of vertical mass flux within cumulus clouds could help clearly distinguish which of these models is most realistic (Ooyama 1971).

The mass flux within cloud is compensated for by subsidence of unsaturated air between clouds, which has different properties. Thus, it is important that vertical mass flux measurements include the cloud volume that contributes significantly to the vertical mass flux

Corresponding author address: Dr. Christopher S. Bretherton, Dept. of Atmospheric Sciences, University of Washington, Box 351640, Seattle, WA 98195.
E-mail: breth@atmos.washington.edu

but exclude as much air between clouds as possible, except that region adjacent to clouds which is part of the turbulent convective circulations.

There have been numerous attempts at calculating the vertical mass flux within cumulus clouds, first with arrays of balloons (Byers and Hull 1949; Braham 1952), then with rawinsondes (Fankhauser 1969, 1974; Betts 1973; McNab and Betts 1978) and instrumented aircraft (Telford and Wagner 1974; LeMone and Zipser 1980; Raymond and Wilkening 1985; Raga et al. 1990). These techniques sample relatively small portions of the cloud over brief intervals of time.

In recent years, Doppler radar has provided the means to determine quantitatively the vertical mass flux with better coverage in time and space. Miller et al. (1982), Frank and Foote (1982), and Raymond et al. (1991) combined multiple Doppler and in situ aircraft measurements to infer vertical mass fluxes in thunderstorms in Colorado and New Mexico. Yuter and Houze (1995) determined vertical mass fluxes within Florida cumulonimbus by analysis of ground-based dual-Doppler radar data. Mapes and Houze (1993) calculated mass divergence profiles from airborne Doppler radar data obtained over equatorial oceans.

The above projects using both aircraft and Doppler radar focused on thunderstorms and convective systems considerably larger than the comparatively shallow cumulus cells found in the trade winds. Since the vertical mass flux profile may vary with cloud size, conclusions drawn from a study of these smaller clouds, in addition to providing valuable insight on their own, complement the studies of the larger-scale systems.

This paper presents results from an observational study of trade wind cumulus clouds that formed off the windward coast of Hawaii during the summer of 1990 using two ground-based Doppler radars and an instrumented aircraft.

2. Experimental setup

As part of the Hawaiian Rainband Project (HaRP 1990), the National Center for Atmospheric Research (NCAR) CP-3 and CP-4 Doppler radars were posi-

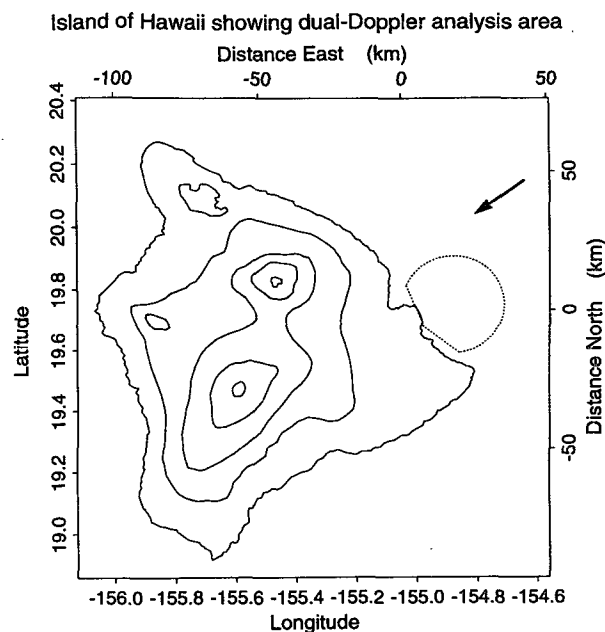Island of Hawaii showing dual-Doppler analysis area

FIG. 1. The HaRP study area. The Doppler analysis area is shown by the dotted curve. CP-4 comprises the origin of the coordinate system. The trade winds (arrow) blow from the northeast.

tioned 17.5 km apart on the eastern coast of Hawaii. The two radars made coordinated coplane scans (Lhermitte 1970) that provided a dual-Doppler lobe extending approximately 30 km offshore. The CP-4 radar, which forms the origin of the coordinate system used in this paper, was stationed at Hilo International Airport, while CP-3 was located southeast of Hilo at a site near the ocean. Table 1 summarizes the characteristics of the two radars. On several occasions, the NCAR Electra flew stacked penetrations through clouds within the Doppler area during coordinated scans, providing helpful comparisons of wind velocity and liquid water concentration and offering near-environment soundings. Figure 1 shows the location of the dual-Doppler lobe with respect to the island of Hawaii.

Our dual-Doppler analysis utilized the software package CANDIS developed by Raymond (1988), with which we interpolated the radial data into a Cartesian grid having a 250-m horizontal and 200-m vertical sampling resolution. Intercomparisons with the NCAR software packages SPRINT (Mohr and Vaughn 1979) and CEDRIC (Mohr and Miller 1983) gave nearly identical results for the mass flux profiles. The rather short baseline of 17.5 km limited the size of the Doppler lobe but established exceptionally high spatial resolution. Most of the clouds examined were within 20 km of the radars, at which distance the diameter of the radar beam was only 0.3 km. Since cumulus clouds drifted through the study area, it was often impossible to follow a single cell through its entire lifespan. However, the great regularity and similarity of clouds forming off Hawaii's

TABLE 1. Characteristics of Doppler radars CP-3 and CP-4.

	CP-3	CP-4
Wavelength (cm)	5.45	5.49
Frequency (MHz)	5500	5460
Peak power (kW)	800	800
Pulse width (μsec)	1.0	1.0
Pulse repetition frequency (Hz)	1500	1500
Antenna area (m^2)	10.75	10.75
Antenna gain (dB)	44.3 ± 0.5	42.3 ± 0.5
Beamwidth (deg)	0.9	0.9
Range resolution (m)	150	150

windward coast partially rectified this shortcoming by providing opportunities to sample numerous cells in all stages of development.

We employed a scatterer fall speed correction $w_t = -2.6Z^{0.107}$ taken from Joss and Waldvogel (1970), where Z is the reflectivity (measured in $mm^6\ m^{-3}$) and w_t is the correction (measured in $m\ s^{-1}$). In addition, we applied a low-pass filter to the velocity data, imposing a half-amplitude wavelength of 2 km (see Raymond 1988), and defined the cloud boundary by a -12 dBZ reflectivity contour. This definition of cloud does not in general conform to the visual outline since it includes radar-observable clear air and precipitation and may exclude cloudy regions that return very weak echoes. The -12 dBZ contour represents the minimum signal strength for which the data provided consistently reliable velocity vectors. The sensitivity of the vertical mass flux calculations to small changes in the reflectivity factor defining cloud boundary was minimal in the cases tested, particularly with respect to the shape of the mass flux profile. Figure 2 compares the mass flux profile of a typical small rainband for cloud boundary values of -12, -10, -8, and -6 dBZ. The derived mass flux varies by up to 30% depending on which threshold is used, but the shape of the mass flux profile does not change substantially with the threshold.

At the top of highly buoyant turrets, the ascending air can slow rapidly from several meters per second to zero, making it difficult to impose a suitable cloud-top boundary condition for the vertical velocity. Hence, we employed exclusively a lower boundary condition that assumed zero vertical velocity at the ocean surface and upwardly integrated the horizontal convergence at each level to calculate the velocities throughout the echo. The cloud tops of Hawaiian trade cumuli were usually below 3 km, so the accumulation of errors by upward integration was less important than for deep convection. In regions where the echo did not reach the surface, CANDIS assumed the horizontal convergence between the surface and the lowest radar-resolvable level was constant and equal to the value at the lowest level. All echoes that included more than a few points of missing data were omitted from this study, with the exception of small clouds in the very earliest stages of development (such as shown in Fig. 3), for which information at the lowest levels was usually unavailable.

3. Background

Trade cumulus clouds develop over much of the subtropical oceans and comprise an important class of convection. Baker (1993) summarizes the observed characteristics of these clouds and discusses their properties.

During HaRP, the height of the trade inversion ranged from an altitude of 1.4 km to an occasional extreme of 3.7 km, having a mean height of 2.1 km. Cloud base varied considerably less, typically forming only
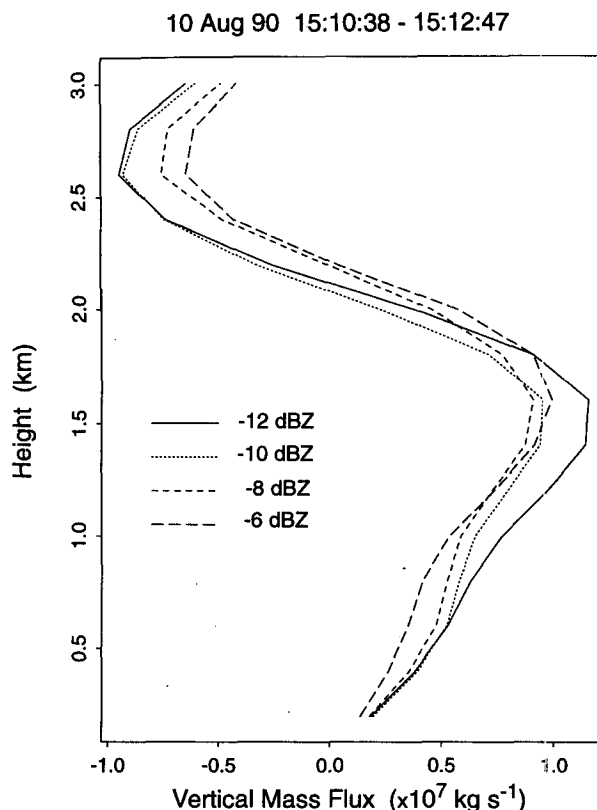

10 Aug 90 15:10:38 - 15:12:47

FIG. 2. Profiles of the vertical mass flux for a rainband that formed on 10 August. The four curves indicate the variation in the vertical mass flux for changes in the reflectivity factor defining cloud boundary. Only those grid points within the echo that have reflectivities greater than or equal to the indicated cloud boundary reflectivity contribute to the vertical mass flux in each of the curves. The sensitivity of the vertical mass flux profile to small changes in cloud boundary reflectivity is minimal.

500 m above the ocean surface. The cells near the island matured quickly, with radar echoes reaching to the surface soon after development, implying rapid formation of precipitation. In this respect, the clouds examined in this paper may not be representative of open-ocean trade wind cumuli, which are often nonprecipitating (Augstein et al. 1973; Holland and Rasmusson 1974). Takahashi et al. (1989) discuss the physics that produces the long-lasting and often heavy rainfall (up to 800 cm yr^{-1}) that characterizes the clouds off Hawaii's eastern coast.

The reflectivity within isolated clouds offshore reached peak values approaching 40 dBZ, and the reflectivity of larger rainbands occasionally exceeded 55 dBZ. Most clouds had attained a reflectivity of at least 5 dBZ in some region by the time the overall signal was sufficient for the computation of three-dimensional air motions. The time required for a cloud to develop, mature, and decay varied from as little as 15 minutes for the smaller cells to several hours for the coastal rainbands.

We calculated the vertical mass flux $F_m(z)$ by integrating the vertical velocity over the horizontal radar-observed cloud area at each level:

$$F_m(z) = \rho(z) \int_{Area} w(x, y, z)dA,$$

where $\rho(z) = 1.0 \exp(-z/8 \text{ km})$ is the air density (assumed to vary insignificantly in the horizontal), $w(x, y, z)$ is the vertical velocity, dA is the area of each horizontal grid point (0.0625 km^2), and Area is the actual horizontal area of the radar echo, which varied with height z.

The vertical velocity represents an indirect measure derived from the horizontal convergence and a lower boundary condition. The vertical velocity at each grid point was calculated by integrating the horizontal convergence surrounding that point, which depended on filtering constraints and interpolation schemes within CANDIS and was subject to significant measurement uncertainty. Small errors in the radial velocity fields sometimes resulted in spurious local convergence and vertical velocity spikes. However, these spikes cancelled when horizontally averaged. Hence, the magnitudes of the individual vertical drafts were less certain than the average taken across the entire horizontal area, which depended only on the echo area-integrated horizontal convergence and was relatively insensitive to the filtering algorithm and measurement errors. Therefore, the total vertical mass flux is a more reliable measure than the separated components of updrafts and downdrafts. For this reason we present only profiles of the total flux.

4. Discussion of reflectivity

In conducting a study of the vertical mass flux, one hopes to measure as much of the circulation within and adjacent to the cloud as possible. The sources of radar backscatter for the warm cumulus cells of Hawaii included cloud droplets, rain, dust, insects, and fluctuations in the refractive index of air. The scattering of radar by hydrometeors and dust is described by Rayleigh scattering theory, provided the radar wavelength is large compared to the maximum particle size (e.g., Battan 1973).

The scattering of radar by inhomogeneities in the refractive index of clear air is considered a form of coherent backscatter, a special case of Bragg's law (e.g., Tatarski 1961; Ottersten 1969; Gossard and Strauch 1983; Doviak and Zrnić 1984). Unlike Rayleigh scattering, much uncertainty continues to shroud its quantitative importance, even though the phenomenon has been observed for over half a century (see Gossard 1990).

A combination of Rayleigh and Bragg scattering made up the observed radar echo. In regions containing large droplets or precipitation, Rayleigh scattering overwhelmingly dominated the reflectivity signal. However, regions of clear air and those that contained only small droplets were often invisible to Rayleigh scattering but sometimes returned a detectable Bragg signal. The uncertainty in the amount of detectable Bragg scattering and its importance in making visible the periphery of small clouds warrants some discussion.

For a range of turbulent eddies within the inertial subrange (Corrsin 1951) the only parameter that characterizes the eddies is the energy dissipation rate. The inertial subrange spans a size range greater the Kolmogorov microscale L_K and smaller than an outer scale L_0. The Kolmogorov microscale is classically defined as (e.g., Broadwell and Breidenthal 1982) $L_K = (\nu^3 \epsilon^{-1})^{1/4}$, where ν is the kinematic viscosity (units of $m^2 s^{-1}$) and ϵ the turbulent kinetic energy dissipation rate ($m^2 s^{-3}$). Baker et al. (1984), in their modeling of turbulent mixing within cumulus clouds, use the quantity $v_L^3 L^{-1}$ to estimate ϵ, where v_L is the velocity characteristic of eddies of scale L. For a typical trade cumulus, the characteristic velocity and size of the largest turbulent eddies are roughly 1 m s^{-1} and 200 m. A value of $1.5 \times 10^{-5} \text{ m}^2 \text{ s}^{-1}$ for the kinematic viscosity of air gives a Kolmogorov microscale on the order of 0.1 cm.

Radars that employ wavelengths comparable to or smaller than the Kolmogorov microscale are sensitive to turbulence scales that are beneath the inertial subrange and tend to be rapidly eliminated by viscous dissipation. Gossard et al. (1984) calculated a critical radar wavelength λ_c below which the pertinent scales are suppressed. They found that for weak turbulence within and above stable layers, λ_c varied from 4 to more than 20 cm. The turbulence resulting from buoyant overturning, however, can be many times more energetic than in stable layers. For $L_K = 0.1$ cm, λ_c for trade cumulus clouds becomes roughly 3 cm. Although this is only an order of magnitude estimate, it is reasonable to conclude that the HaRP radars with wavelengths of 5.5 cm were capable of observing Bragg scattering from at least some of the turbulence structure.

Rogers et al. (1992) compared the reflectivity measured by a 33-cm wavelength vertically pointing wind profiler to the reflectivity simultaneously measured by the collocated NCAR CP-3 radar for three time periods during HaRP. The longer wavelength of the profiler perceived a reflectivity approximately 29 dB greater than the 5.5-cm radar, a value that agrees well with the amount predicted by Bragg scattering theory. They concluded that the observed reflectivity of the trade inversion for both the profiler and the 5.5-cm radar was consistent with, and explained by, Bragg scattering.

Knight and Miller (1993) compared time-lapse photography of early cumulus development with corresponding 5.5-cm radar images from HaRP and concluded that, as a result of Bragg scattering, all clouds visible to the eye produced detectable radar signals when examined at close range. Their data also indicated

that the visible cloud outline corresponded to a radar reflectivity of about −10 dBZ, and clear air thermals beneath cloud base were sometimes discernible through Bragg backscatter long before the onset of precipitation.

In this study, we made an attempt to determine the importance of Bragg backscatter by comparing the liquid water measurements recorded by nearly simultaneous collocated aircraft to the observed radar reflectivity. In five cases, the aircraft encountered cloudy regions where no droplets were larger than 32 μm, which constituted the upper particle size limit measurable by the forward-scattering spectrometer probe (FSSP) (Dye and Baumgardner 1984; Baumgardner et al. 1985; Baumgardner and Spoward 1990). For these cases, the reflectivity resulting from the 15-channel FSSP spectrum using Rayleigh scattering theory varied between 6 and 15 dB less than the total reflectivity measured by radar when the maximum echo strength was approximately −6 dBZ. Although HaRP provided too few cases for a proper statistical treatment, the results nevertheless suggest that Bragg scattering accounted for a significant portion of the returned signal at low reflectivities for some of the Hawaiian echoes. In one such case, the contribution of Bragg scattering more than doubled the size of the scan volume over which mass flux calculations could be made.

However, despite contributions of Bragg scattering, examination of very small cells demonstrated limitations in the capability of the radars to observe some cloud-induced mass fluxes. The following section presents two examples of data retrieved during this project. The first is of one of the smallest isolated cells, and the second is of a rainband.

5. Case studies

a. Small isolated cell

During the morning of 24 July, a small cumulus cell developed 21 km east of Hilo and remained separated from its nearest neighbors by approximately 10 km of clear air. The cloud was one of the smallest and hence fastest evolving of the cells, persisting for only 18 minutes before dissipating. We present it because it was one of the few clouds that remained within the dual-Doppler lobe over its full life cycle. This case also illustrates that despite the contributions of Bragg scattering, not all of the mass flux is seen by radar at low levels.

Figure 3 plots contours of reflectivity in intervals of 5 dBZ, beginning at −5 dBZ, for both horizontal and vertical cross sections for four time periods spanning the cloud's lifespan. The occasional incompleteness of the first reflectivity contour is an artifact of the plotting routine and does not necessarily indicate missing data. The figure includes Doppler velocity vectors observed within the −12 dBZ echo. All times are given in UTC.

The first time period shows the earliest radar-observable stage of cumulus development for which mass flux calculations could be made. The maximum reflectivity was just under 5 dBZ and the vertical cross section reveals no echo beneath an altitude of 0.8 km, even though cloud base was typically at 0.5 km. Turbulent fluctuations in refractive index in the lower part of the cloud were insufficient to be detectable by the HaRP radars, and precipitation had yet to commence. This example illustrates an extreme case of missing information at low levels. In this instance, we have no way of satisfactorily estimating the flux below and near cloud base or determining the effect of the missing information on the mass flux profile at higher levels.

The third time period displays the echo at its maximum intensity, when it returned a peak signal of almost 15 dBZ. Contours of reflectivity extend to the surface, suggesting precipitation. At upper levels on the leeward side, the velocity has a large vertical component. Note that a detectable echo only occurs above 1.2 km in this grid column. To assign a vertical velocity, the measured horizontal convergence at 1.2 km is extrapolated down to the sea surface, probably an unrealistic assumption for this case and one that also renders w very sensitive to errors in Doppler radial velocities at 1.2 km. To prevent bad data or assumptions from excessively biasing mass flux calculations, we excluded all edge points with updrafts larger than twice the mean vertical velocity over updrafts at the same level that were stronger than 1 m s^{-1}. We applied an analogous filtering procedure to edge downdrafts.

The fourth pair of images reveals the echo during its decaying stage. The cell had completely dissipated by the next available scan, three minutes later. Visual inspection of images such as these showed that for small cumuli, a significant fraction of the vertical mass flux was associated with reflectivities less than 0 dBZ for which Bragg scattering may have played a role. For cloud groups and rainbands, the weak reflectivity regions contributed less to the total mass fluxes.

Figure 4 presents a chronological sequence of the vertical mass flux profile for six time periods spanning the cloud's life cycle, four of which were included in Fig. 3. The vertical axis on the left gives the height above the ocean surface in kilometers and on the right the same height measured in standardized nondimensional units defined such that zero represents cloud base and unity the base of the trade inversion: $Z_{\text{Non-dim}} = (Z - Z_{\text{Cld Bse}})/(Z_{\text{Inv}} - Z_{\text{Cld Bse}})$.

The first two curves of Fig. 4 illustrate the early stages of convection when the cloud exhibits strongly positive mass fluxes that reach a maximum just beneath the trade inversion. The profiles suggest rapid net entrainment below an altitude of 1.3 km. However, the rate of entrainment in these early stages is exaggerated by the underestimation of mass flux below 800 m, seen in Fig. 3.
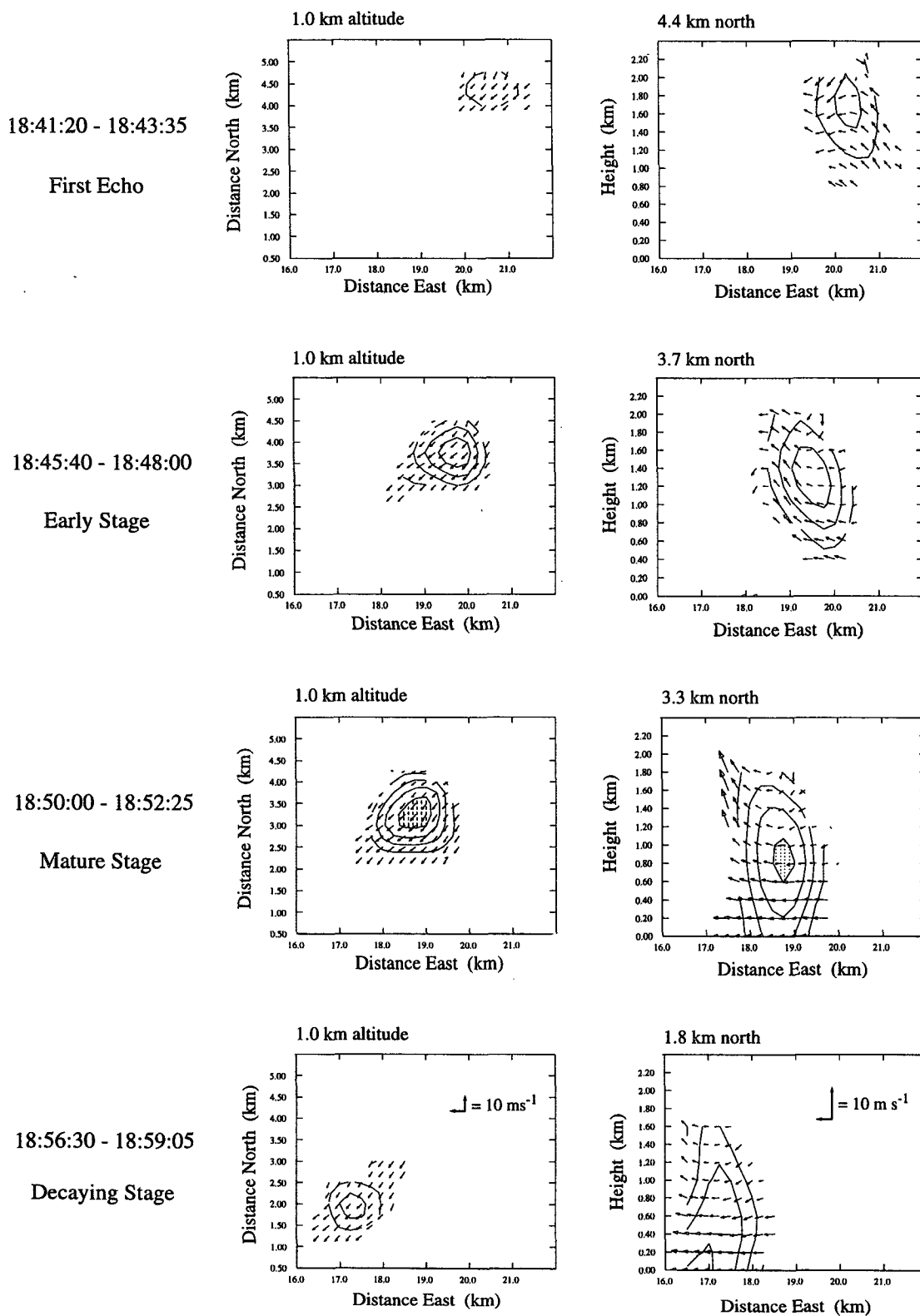
FIG. 3. A chronological sequence of four scans through a small isolated cell that formed on 24 July showing horizontal cross sections at a height of 1.0 km (left image) and vertical cross sections through the echo centers (right image). The reflectivity is given in contours of 5 dBZ beginning at −5 dBZ; shaded regions indicate a reflectivity greater than 10 dBZ. For clarity, the vertical scale in the vertical cross sections is twice the horizontal. Velocity vectors overlie the reflectivity contours; the common scale for each column of plots is shown in the lower images.

24 July 1990   18:41 - 18:59   Small Isolated Cell

1) 18:41   2) 18:45   3) 18:50
4) 18:52   5) 18:54   6) 18:56
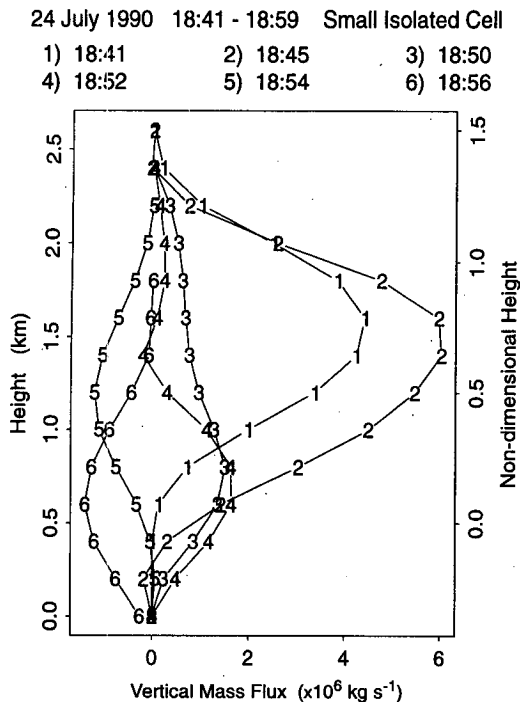
FIG. 4. The vertical mass flux calculated in the 24 July cell at six time periods, four of which were shown in Fig. 2. The left axis gives the height above the ocean in kilometers, the right a nondimensional height where zero represents cloud base and unity the base of the trade inversion.

With the commencement of precipitation in the third time period, at least part of the motion below cloud base became visible. The third time period reveals a net mass flux below cloud base that is slightly positive, implying that the updrafts fueling the convection were still stronger than the downdrafts resulting from precipitation drag and evaporative cooling.

The fourth time period marks the beginning of decay where the echo had reached its maximum size of 9 km^2 and commenced to shrink. In the latter three time periods, the altitude at which the vertical mass flux manifests peak negative values propagates downward. In the fourth curve, the altitude of greatest negative mass flux is roughly 1.4 km. By the sixth time period, that altitude has descended to a mere 0.6 km, which is just above cloud base. This behavior agrees with prior visual and aircraft observations of the later stages of cumulus clouds, where precipitation dominates and upward convection weakens, and the clouds give the appearance of collapsing in on themselves.

b. Rainband

The second example is of a rainband that formed on the morning of 10 August approximately 25 km offshore. Figure 5 shows horizontal cross sections of the rainband at an altitude of 1.0 km for two time periods

separated by one-half hour. Figure 6 gives vertical cross sections of the same rainband. In comparison to the small isolated cell, the rainband evolved much more slowly and remained more localized in position. Individual cells embedded within the band retained their identity for relatively long periods of time.

Figure 7 provides profiles of the vertical mass flux for the images shown in Figs. 5 and 6, plus a third profile at an intermediate time. All three curves are very similar in shape, despite the evolution from a growing echo (early stage) in the first curve to an echo of constant size (mature stage) in the later two. In this example (but not in general), the series of vertical mass flux profiles show little difference between stages. Substantial negative mass fluxes near the cloud top suggest that entrainment of air by overshooting cumulus tops from above is quite important.

6. Results

A set of coplane scans sufficient for the analysis of three-dimensional air motions spanned less than three minutes and hence provided a means of documenting the evolution of even the shorter-lived cells. The change in a cloud's size and reflectivity between successive scans gave information on its developmental stage. In this paper, we define three cloud phases: early, where scans show the echo to be growing or intensifying; mature, where the area and reflectivity remain nearly constant; and decaying, where scans reveal an echo that dissipates in time. We divide the data into isolated cells that cover less than 30 km^2 and are separated from each other by at least 5 km of clear air and cloud groups and rainbands that occupy more than 50 km^2. For rainbands, which often drifted over shore and out of the dual-Doppler lobe in their later stages, single radar surveillance scans helped discriminate the evolution of the echo area. Cloud groups typically consisted of two to five loosely connected cells, which were sometimes separated by as much as several kilometers of clear air. Cloud groups often intensified into rainbands as they drifted coastward and frequently made up the earliest stages of the larger cloud category. The isolated cells, on the other hand, nearly always dissipated before merging with other clouds. Figure 8 shows the composite results of the vertical mass flux per unit area of echo plotted against a standardized nondimensional height for each of the two size categories. Each curve is an average of between 35 and 153 scans, depending on the number of qualifying cases found in each phase. Clouds only rarely penetrated to heights above a nondimensional value of 1.5, so the upper portion of the plots describes a relatively small fraction of the total cloud area (see Fig. 9).

The results shown in Fig. 8 confirm that the vertical mass flux per unit area is a strong function of the cloud's evolutionary state. In addition, the similarity in the shape of the mass flux profiles for the two size

1.0 km altitude 15:10:38 - 15:12:47　　　　1.0 km altitude 15:40:13 - 15:42:27
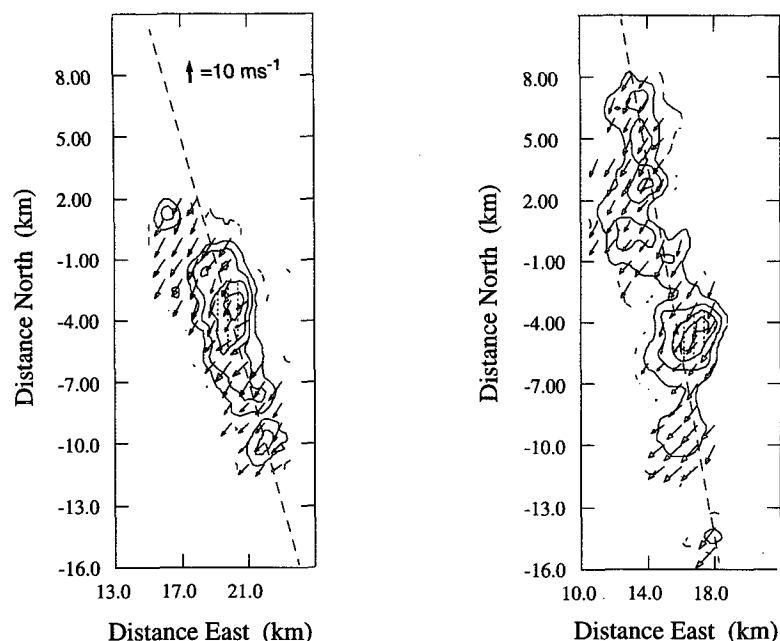
FIG. 5. Horizontal cross sections of a rainband that formed on 10 August for two time periods separated by 29 minutes. Reflectivity contours begin at 0 dBZ and are separated by 10 dBZ, and vertical shading indicates values greater than 20 dBZ. The dashed line defines the vertical plane for the images in Fig. 6.
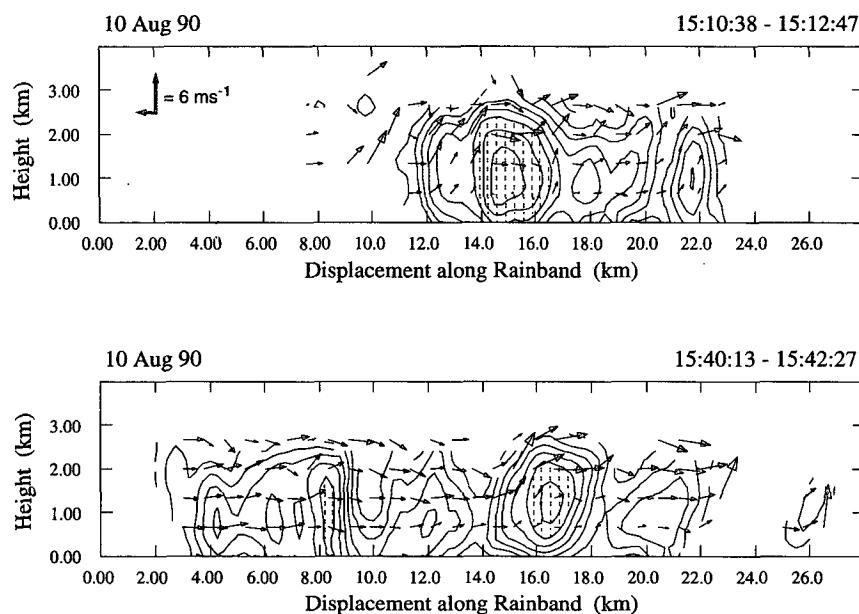
10 Aug 90　　　　　　　　　　　　　　　　　　　　15:10:38 - 15:12:47

10 Aug 90　　　　　　　　　　　　　　　　　　　　15:40:13 - 15:42:27

FIG. 6. Vertical cross sections of the rainband given in Fig. 5 with reflectivity contours beginning at 0 dBZ and separated by 5 dBZ. The lower axis gives the displacement along the dashed line shown in Fig. 5, beginning at the north. For clarity, the vertical scale is twice the horizontal; the common scale for the velocity field is shown in the upper plot.

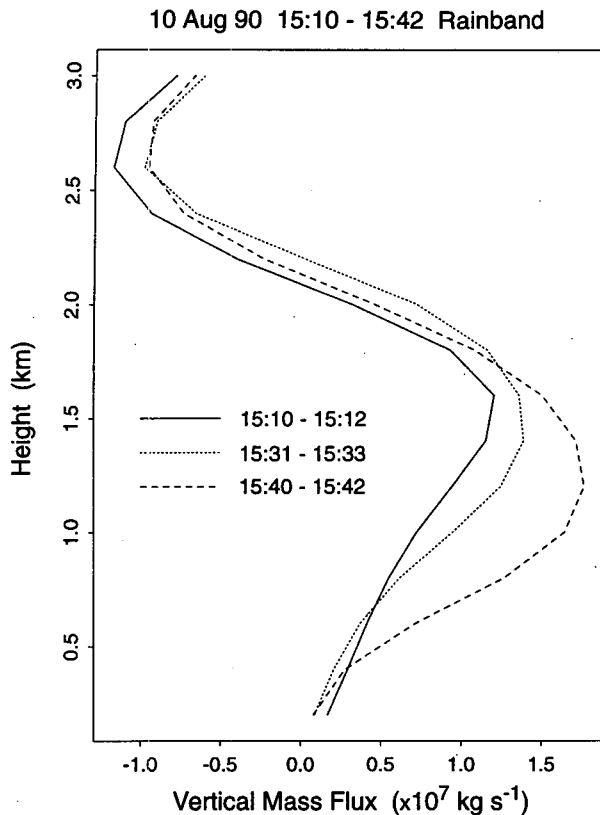## 10 Aug 90 15:10 - 15:42 Rainband

FIG. 7. Profiles of the vertical mass flux in the rainband at the times shown in Fig. 5 and at an intermediate time.

categories suggests that the organization of component cumulus cells into a larger convective body does not significantly alter the mass flux profile.

On the other hand, the magnitude of the vertical mass flux per unit area for the smaller cells is nearly twice that of the cloud groups and rainbands. One explanation may be that the larger cloud bodies, which are typically composed of numerous active cells, are less vigorous per unit area because only a portion of the whole cloud actively participates in the vertical transfer of mass, at any given time, as appears to be the case in larger convective systems (Yuter and Houze 1995). The longer-lived rainbands, which produce greater liquid water contents, stronger convection, and more copious precipitation, probably contain inactive but radar-detectable regions that, if around the individual cells, would have quickly evaporated. A second possible explanation for the difference in magnitude of the mass fluxes is that cloud groups and rainbands contain cells in varying stages of development, so that, for example, decaying cells may be included in a growing echo. However, the similarity in shape of the mass flux profile between the two size categories and the same factor of 2 difference in the average flux taken over all three developmental stages (see Fig. 10) suggests that the

coexistence of varying developmental stages is not a primary factor.

The region of negative mass flux in the curves representing the mature stage probably reflects the collapse of penetrative turrets formed in the early stage. During the decaying stage, that collapse continues to descend in altitude, attaining a maximum at the base of the inversion. The combination of negative buoyancy induced by evaporative cooling at cloud top and precipitation-driven downdrafts at lower levels probably accounts for the downward propagation of peak negative values in the mass flux profiles, which is shown clearly in the 24 July case study.

In addition to examining variations in the vertical mass flux resulting from cloud size and phase, we compared cases according to the height of the base of the trade inversion, the time of day, and the convective available potential energy (CAPE) as measured by aircraft soundings. Gathering a statistically robust set of cases in which only one of the variables changed proved difficult. The few cases available did not show obvious variations in the vertical mass flux profiles as a function of any of these variables.

Figure 9 shows the vertical profiles of cloud area for the two size categories. The area decreases rapidly above the inversion, particularly for the smaller isolated cells. In both cases, the clouds in the early stage of development exhibit proportionally greater area above the inversion, a feature consistent with penetrative turrets that sometimes extend a considerable distance above the base of the trade inversion.

The early stage rainbands and cloud groups had the largest average area within the dual-Doppler lobe, in apparent contradiction to our definition of the evolutionary stages. This is because rainbands often stretched along much of Hawaii's eastern coast, frequently extending well out of the Doppler analysis area. Rainbands were therefore inherently only partially observable. The mature stages of cells and rainbands were defined as those echoes that occupied the greatest average areas in single-radar surveyance scans. Rainbands tended to drift over the shore and out of the Doppler lobe as they developed, leaving a smaller echo area within the Doppler lobe during the mature and decaying stages.

The convective elements making up the rainbands had typical areas 25 to 50 km^2, and several such elements were sampled in each scan, enough to represent the shape of the mass flux profiles. Cloud groups, which are included with rainbands in the composite profiles, were smaller in size but were observed equally well in all phases of development.

In order to compare the vertical mass flux averaged over all three phases for the two size categories, we normalized the areas of the mature and decaying phases for the cloud groups and rainbands so that the maximum cloud area for each profile was equal to the maximum area of the early stage, which was better sampled.
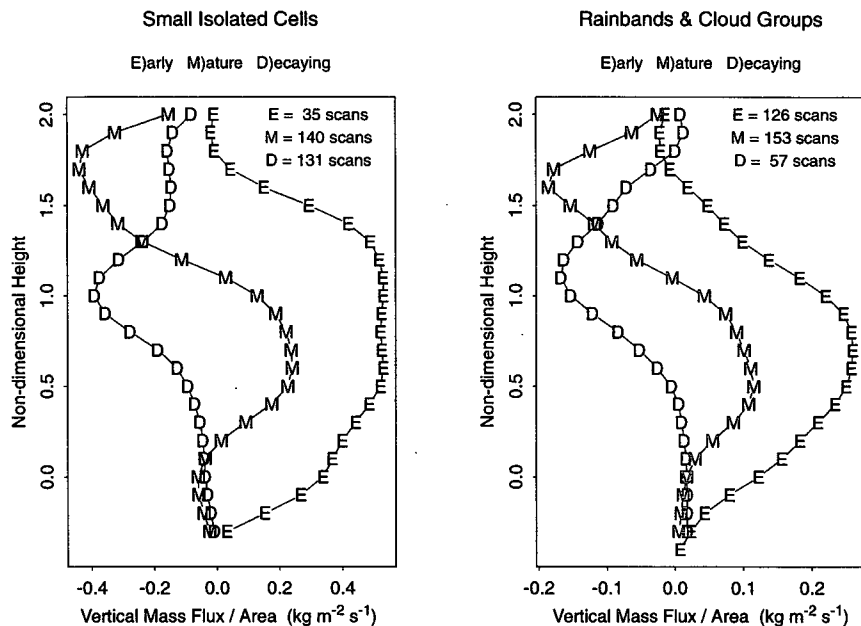
FIG. 8. Profiles of the average vertical mass flux per unit area plotted against a standard non-dimensional height and categorized by size and phase. Small isolated cells represent clouds that achieved a maximum area of 30 km² or less and were separated from nearest neighbors by at least 5 km of clear air. Cloud groups and rainbands occupied 50 km² or more. The early, mature, and decaying stages each comprise an average over a different number of scans, depending on the number of qualifying cases found.
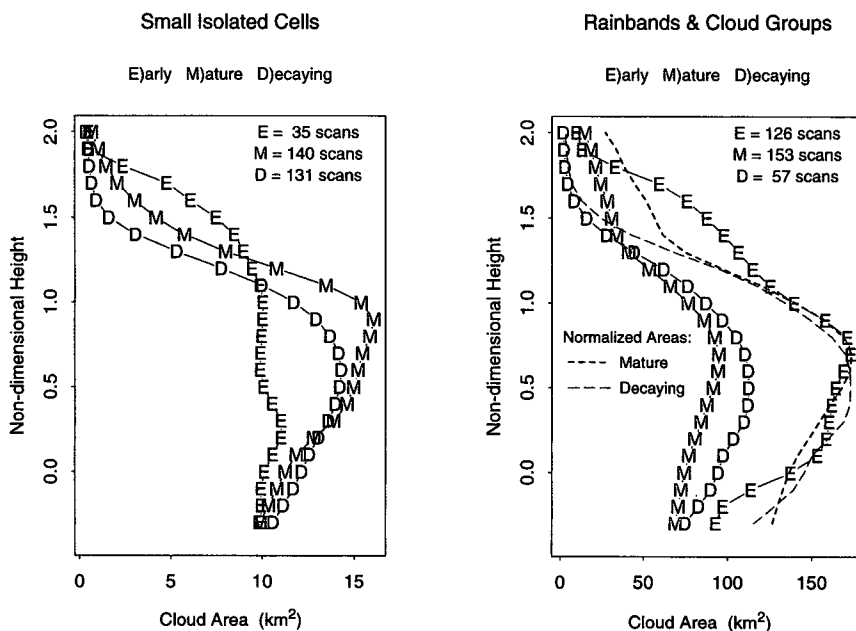

FIG. 9. Profiles of the average cloud area, similar to Fig. 4. Less of the rainbands were observable in the mature and decaying phases because they tended to drift shoreward and out of the Doppler lobe. The short-dashed (long-dashed) line represents the mature (decaying) profile after being normalized to have the same maximum size as the early stage.
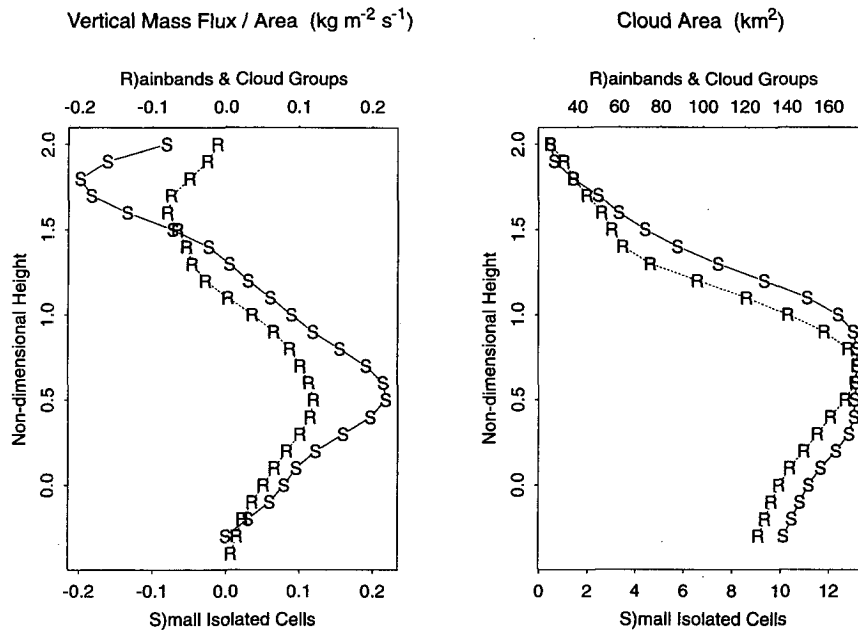
FIG. 10. The average overall phases of the unit area vertical mass flux and cloud area, assuming each phase contributes equally to the average. The lower axis gives the magnitude for the small isolated cells (S); the upper axis the magnitude for the rainbands and cloud groups (R).

Although this does not take into account the larger area typical of the mature stage, we believe it is less haphazard than assigning an arbitrary value, such as one based on the area of the isolated cells, which may have varied considerably more than the larger rainbands. Although surveillance scans helped discriminate the phase of the rainbands, they did not prove satisfactory as a basis for normalization. The normalized profiles are shown in Fig. 9 as short-dashed (mature) and long-dashed lines (decaying).

Figure 10 presents the average overall phases of the vertical mass flux per unit area and the cloud area, using the normalized profiles of area. Both size categories trace curves of nearly identical shape for both plots, but the rainband profile shows somewhat weaker values.

Figure 11 combines the results of Fig. 10 into a single profile of the total life-averaged vertical mass flux for the two size groups, weighting the three stages equally. The maximum vertical mass flux occurred at midlevels at a nondimensional height of approximately 0.5 (at a height of roughly 1.3 km above the ocean surface). The rapid decrease of upward mass flux with decreasing height below this level is consistent with precipitation-driven downdrafts. However, some of the decrease may result from exaggerated lateral entrainment due to unseen air motion at the lowest levels in the early stages. The highest segment of the curves shown in Fig. 11, representing regions well above the inversion, illustrates net downward mass flux. This probably reflects entrainment of air from above the in-

version into overshooting turrets that collapse after mixing and carry the gathered mass downward.

One concern in producing the average mass flux profiles is the uncertainty in the average duration of each phase in a typical cloud's life cycle. Since cumulus cells drifted into and out of the Doppler analysis area, we found it difficult to judge the characteristic duration of each evolutionary state. The all-phase average of the vertical mass flux implicitly assumes that each stage is equally important. A study of clouds observed for longer times using single-radar observations could better resolve this issue.

7. Discussion

Vertical profiles of the vertical mass flux in shallow precipitating cumulus clouds are similar both in structure and evolution to thunderstorms and mesoscale convective systems: near zero or even negative net mass flux below cloud base, with a maximum positive flux at higher levels. Braham (1952), Lemone and Zipser (1980), Frank and Foote (1982), Houze (1989), Raga et al. (1990), Raymond et al. (1991), Yuter and Houze (1995), and others all present mass flux profiles that are similar in shape despite substantial differences in information-gathering strategies, project locations, and analysis techniques. Our results differ from those obtained for deep convection, where the maximum flux is typically found higher up in the convecting layer. Thus, trade cumulus clouds should exhibit less of a

Vertical Mass Flux (×10⁷ kg s⁻¹)
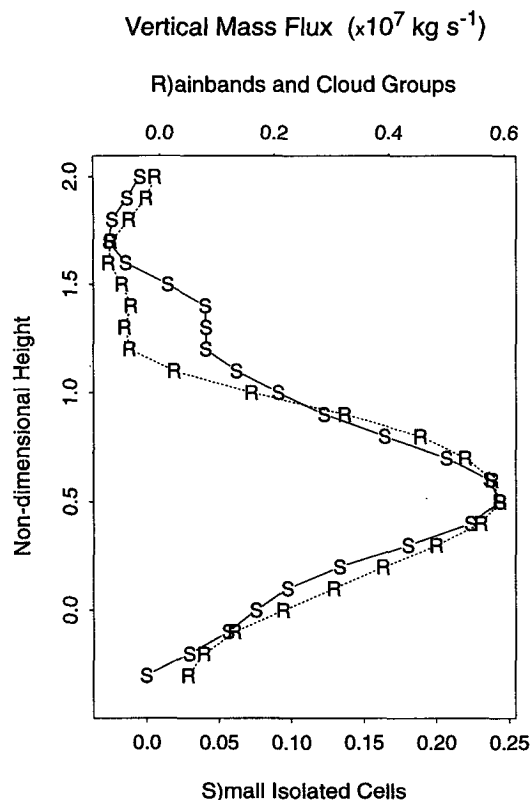
R)ainbands and Cloud Groups

FIG. 11. The all-phase average of the total area-integrated
vertical mass flux for the two size categories.

tendency to develop in the proximity of their neighbors
(Mapes and Houze 1993). If the stratiform region is
excluded from the deep convection mass flux, the re-
sults are more similar.

Houze (1982) examined the evolution of the average
vertical motion in tropical cloud clusters during GATE
and found a progressive upward propagation of the
level of maximum mean upward motion over time. For
the large tropical clusters, this upward shift in peak
mass flux occurred over a span of several hours. We
observed a similar phenomenon in the smaller trade
cumulus clouds during HaRP, though over much
shorter timescales.

Our observations are surprisingly different from the
mass flux profiles deduced for nonprecipitating trade
cumuli over the Caribbean Sea during BOMEX. Both
budget studies (Betts 1975) and an ensemble cloud
model (Siebesma and Cuijpers 1995) show large mass
transport just above cloud base, which decreases rap-
idly with height up to the trade inversion. The differ-
ence between our observations and those of BOMEX
probably results from rapid destabilization of the HaRP
boundary layer due to forced mean lifting upwind of
the island, which encouraged a much larger fraction of
cumuli to ascend into the trade inversion. It is also pos-

sible that the HaRP radars could not detect the shallow-
est clouds.

8. Comparisons with numerical models

We compared our observations to a three-dimen-
sional large eddy simulation (LES) model and a buoy-
ancy sorting conceptual model of an isolated cumulus
cloud. The observations agree much better with the
LES model results than with those of typical conceptual
models, including the buoyancy sorting scheme. While
the cumulus cloud simulated by our LES is deliberately
simplified from the observed convection both in initi-
ation and organization, our purpose in this section is
simply to show that the mass flux profiles in the three
observed evolutionary stages, as classified based on
rate of change of echo size, correspond well to stages
in the temporal evolution of a single isolated cumulus
cloud.

The University of Washington LES model integrates
the anelastic equations (Ogura and Phillips 1962) mod-
ified to include vapor–liquid phase changes and a mod-
ified Kessler parameterization (Chen and Cotton 1987)
for rain. The prognostic variables include the liquid wa-
ter potential temperature θ_l, mixing ratio $q_t = q_v + q_c$
in the form of vapor and small cloud droplets, rainwater
mixing ratio q_r, momenta, and an arbitrary number of
user-defined scalars. These variables are advected us-
ing a Leonard et al. (1993) forward in time multidi-
mensional conservative advection scheme with flux
corrections (Zalesak 1979) and source terms that are
treated following Smolarkiewicz and Margolin (1993).
No explicit subgrid-scale turbulent diffusion is in-
cluded. Stevens (1994) describes the model in detail.

To determine the mass flux profiles that typify a cu-
mulus cloud in a given sounding, we initiated a cloud
in the LES model as follows. In a horizontally homo-
geneous atmosphere, we increased q_t by 0.3 g kg⁻¹ and
θ_l by 0.5 K in a spherical bubble of air of radius 300
m, centered 300 m above the ground. These perturba-
tions are similar to those observed underneath active
cloudy updrafts in a trade cumulus boundary layer
(LeMone and Pennell 1976). The properties of the
cloud that evolved were mainly driven by the condi-
tional instability of the sounding and did not vary sig-
nificantly with 0.1 g kg⁻¹ or 0.1 K changes in the bub-
ble properties. For the simulations presented here, we
used a 6 km by 6 km wide by 3 km deep domain with
a grid spacing of 75 m in all directions and a time step
of 5 seconds. The observed sounding (which included
a very shallow layer of dense island outflow air below
50 m) was modified slightly to reflect open ocean con-
ditions by homogenizing all of the air between 50 and
500 m and replacing the outflow layer below by the
homogenized air from above. This change removed sta-
ble stratification from below cloud base in the observed
sounding that otherwise suppressed convection in our
model runs. In reality, the upward forcing of air at the

convergence line where the island outflow encounters the oncoming trade winds probably initiated cloud formation.

The mass fluxes were computed every 5 seconds as the density-weighted horizontal integral of vertical velocity across the "cloud mixed region." The cloud mixed region is the volume of air that either contains cloud or has undergone a noticeable amount of turbulent mixing as a result of circulations induced by the cloud.

We deduce the region of turbulent mixing from a conserved variable diagram (Paluch 1979; Smolarkiewicz and Bretherton 1989) as follows. At the beginning of the simulation, we define two passive tracers: the ratio ξ of the initial parcel height to the domain depth and $\eta = \xi^2$. The key point is that initially at all points the value η of the second tracer is nonlinearly related to the value ξ of the first tracer at that same point. In the real physical system, advection alone would preserve the relation $\eta = \xi^2$. However, if both tracers are linearly mixing, a mixture of air from two initial heights will lie on the mixing line connecting its endpoint tracer values on a conserved variable diagram of η versus ξ, which is above the curve $\eta = \xi^2$. In general, for any mixture of air from different initial heights, the mixing indicator $D = \eta - \xi^2 > 0$.

If this approach is to be used to diagnose the cloud mixed region in a numerical simulation, the advection scheme must be "conservative," that is, exactly conserve the discrete volume integral of any advected tracer, which our scheme does. In this case, both ξ and η are linearly mixed in the high gradient regions produced by cloud circulations. This mixing is due to numerical diffusion by the flux-corrected transport scheme, even though there is no explicit diffusion in the model. We include all air where $D > 0.01$ (turbulently mixed air) or $q_l > 0$ (air in the cloud updraft which has not yet undergone mixing) in the cloud mixed region.

Our simulation ran for 25 minutes, by which time the cloud ceased to evolve and the vertical velocity field became stagnant. The mass flux distribution in the simulation went through three stages similar to those found in our observations: after 10 minutes the model cloud mass fluxes resembled the early stage, after 15 minutes the mature stage, and after 20 minutes the decaying stage. Figure 12 shows profiles of the vertical mass flux averaged over ten minutes centered around these times. For comparison, Figure 13 gives the observed vertical mass flux profiles for small isolated cells (obtained by combining the profiles in Figs. 8 and 9). A limitation of our simulations was that the simulated cloud area (0.8 km^2 at 10 minutes and 1.9 km^2 at 20 minutes) was smaller than the mean area of the isolated cells examined in this study by a factor of 10. The shape of our observed mass flux profiles was found to be independent of the area of the cloud, so our simulations may nevertheless have relevance to the observed clouds.

3-D Boundary Layer Convection Model
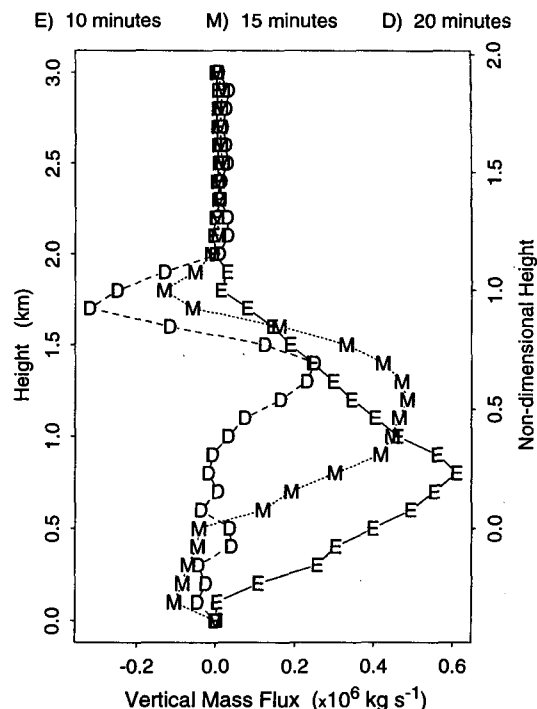
E) 10 minutes   M) 15 minutes   D) 20 minutes

FIG. 12. Three-dimensional LES simulation of a small isolated cloud. The three curves portray the vertical mass flux profile for 10-min averages surrounding 10, 15, and 20 minutes, which correspond to the early, mature, and decaying stages. The areal coverage of the model cloud was a factor of 10 less than the mean size of the observed clouds, reducing the magnitude of the calculated fluxes by that amount.

The mass flux profiles predicted by the model are similar in shape to those of the observed clouds, especially in the mature phase. Our radar-deduced phase classifications were based purely on whether the overall echo area of a cloud or system was increasing, steady, or decreasing. The model results support the contention that the "early" stage in the observations is in fact dominated by young cumuli, while the "mature" and "decaying" phases are dominated by individual cumuli that are mature or decaying, respectively.

Differences in the mass flux profiles between radar and LES reflect limitations of the radar observations, the idealized nature of the simulation, and differences between the classification schemes used for the model and for the radar observations. In the early phase, the modeled mass flux is concentrated in the lower part of the cloud layer, in contrast with observations. This difference may be due to a failure of the radar to observe an echo until after the cloud had grown several hundred meters deep. It may also result from subcloud turbulence and mechanical forcing that existed in the HaRP boundary layer but were not included in the LES simulations. After 20 minutes, the model shows intense
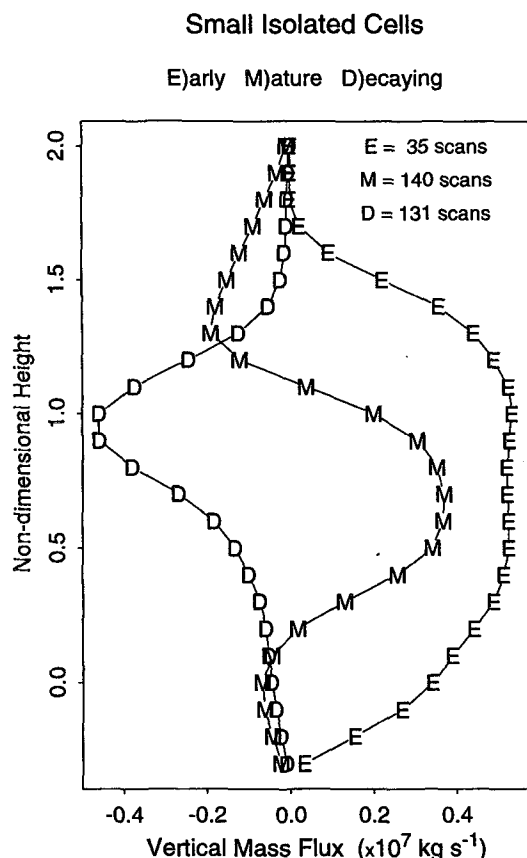
Small Isolated Cells

E)arly M)ature D)ecaying

E = 35 scans
M = 140 scans
D = 131 scans

FIG. 13. The observed vertical mass flux for small isolated cells obtained by combining Figs. 4 and 5.

We also ran a simulation in which precipitation was suppressed (shown by the dotted line in Fig. 14). This had a surprisingly small impact on the lifetime-averaged fluxes. This lends credence to the hypothesis that our mass flux profiles differ from those of BOMEX more because of the different cloud size spectrum rather than because the HaRP cumuli were heavily precipitating. Most of the HaRP cumuli grew to the trade inversion, while results of Siebesma and Cuijpers (1995) suggest that most BOMEX cumuli were quite shallow.

A major purpose of producing mass flux profiles is to validate simple conceptual models of cumulus transport. We compared our observations and LES runs with two such models. Our observations show maximum net upward mass fluxes midway between cloud base and the inversion due to a partial cancellation of radar-observed updraft and downdraft mass fluxes below this level. The LES results have more mass fluxes at low levels and less near the inversion. Neither is consistent with an entraining plume model, for which the mass

Vertical Mass Flux Averaged Over Lifecycle

O)bservations   (units 10^7 kg s^{-1})
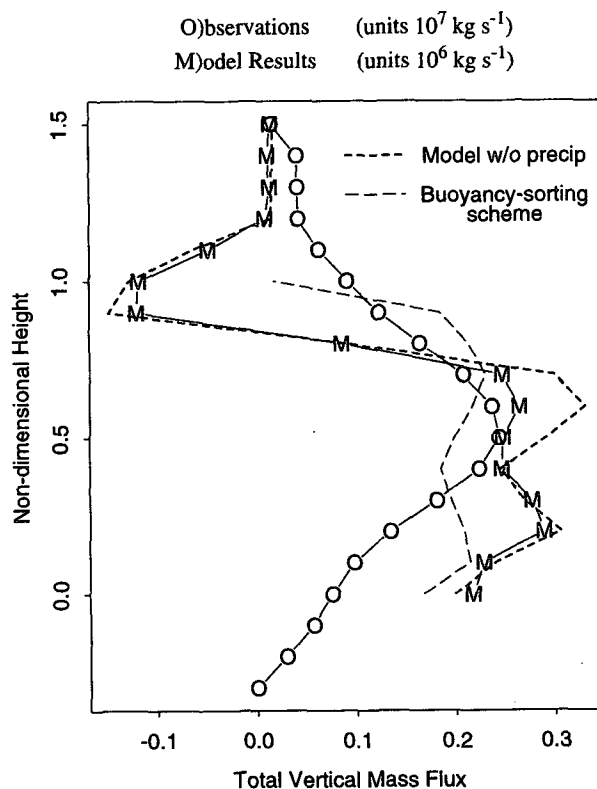M)odel Results   (units 10^6 kg s^{-1})

FIG. 14. A comparison of the vertical mass flux profile averaged over the cloud's life cycle for the LES model (M) and radar observations (O). The dotted curve shows an LES run with precipitation suppressed, and the dashed line the results of a buoyancy sorting model (arbitrary units).

negative mass flux at the inversion, similar to our decaying phase observations, which in the model run is due to turbulent entrainment and evaporative cooling at cloud top. However, latent heating predicted by the model produces net positive mass flux just below this level, in contrast with observations. A more realistic simulation of an ensemble of cumuli, using a nested grid to embed an inner domain covering the dual-Doppler region in an outer domain describing the mesoscale flow around Hawaii, could be used as the basis of a more detailed comparison of model and observations, including the echo structure as well as the mass fluxes.

In Fig. 14, the total vertical mass flux (M) of the modeled cloud averaged over the duration of the simulation is compared with the mass flux profile (O) for small isolated cells taken from Fig. 11. The agreement is not as good as for the individual evolutionary phases. Near cloud base, the observed net vertical transport is only one-half as large as in the model. This again suggests that some of the updrafts do not produce a detectable echo, leading to an underestimate of low-level convergence. The model simulation also displays net negative mass flux just beneath the inversion, which was not seen in the observations.

fluxes would increase with height up to a detrainment level at the plume level of neutral buoyancy. This level would be in the inversion at a nondimensional height between 1 and 1.2, depending on the assumed lateral entrainment rate, and is much higher than the observed level of maximum mass fluxes. The disagreement is largely due to the contributions to the overall mass flux from the mature and decaying phases, where evaporation and precipitation-driven downdrafts (not included in an entraining plume model) are important. This underlines the need to base cumulus parameterizations on conceptual models that average overall evolutionary phases of cumuli.

The dashed curve in Fig. 14 is a mass flux profile predicted by a buoyancy sorting scheme that includes precipitation processes but not reevaporation of rain into the underlying air (Raymond and Blyth 1986, 1992). The buoyancy sorting scheme implicitly recognizes the lifecycle of a cumulus cloud by following the mixing and precipitation processes that occur within its component air parcels while they move to their level of neutral buoyancy. Two precipitation-controlling parameters must be specified in this scheme: the temperature T_c below which the formation of rain is assumed to begin, and a parameter R_p that determines the conversion rate of liquid water to rain. We chose $T_c = 281$ K, corresponding to the ambient temperature 500 m above cloud base, and $R_p = 0.014$. We found weak sensitivity of the mass flux profiles to small changes in T_c and R_p. We used the same environmental sounding and cloud-base air properties as in the LES model runs. The mass fluxes predicted by the buoyancy sorting model are quite uniform with height and agree well with the early phase of our observations. They compare less well with the observed mass fluxes averaged over the cloud's lifetime. They agree well with the LES results below a nondimensional height of 0.75, but unlike in the LES they are maintained all the way up to the inversion base. It is possible that the buoyancy sorting model is underestimating the downward mass transport due to penetrative downdrafts driven by evaporative cooling in decaying turrets. This suggests that the buoyancy sorting parameterization may need to include enhanced entrainment in overshooting cumulus turrets in addition to the current inclusion of lateral entrainment.

Our observations constrain the idealized models of shallow cumuli used in cumulus parameterization schemes and help quantify the substantial role of downdrafts. While the comparison is limited due to uncertainty in the interpretation of our observed mass fluxes, the observation–LES comparison suggests that the mass fluxes evolve in a manner similar to the life cycle of a single isolated cumulus, even when the cumuli are organized into groups or lines. The downdrafts associated with collapsing turrets are underestimated by the two idealized models of cumulus clouds we considered.

9. Conclusions

Our Doppler radar measurements of Hawaiian trade cumuli indicate that their vertical mass flux profile undergoes a characteristic evolution that is relatively independent of cloud size and organization. The observed evolutionary pattern, in which updrafts dominate initially but are replaced by downdrafts first at the inversion and then also lower down in the cloud, is consistent with many previous studies of trade cumulus clouds, but radar analysis allows a much larger sample of shallow cumuli, both isolated and organized, to be analyzed than in previous studies based on aircraft penetrations. In addition, the radar accurately measures echo-integrated horizontal convergence, while aircraft studies must extrapolate their measurements from the flight line to area or volume averages over an entire cloud, introducing large uncertainties. However, cloud-associated vertical motions near the updraft base, outside the cloud edges, and in other echo-free regions are not included in our analysis. We have found that these motions may be important, particularly for small isolated cumuli early in their evolution.

Averaged over the radar echo lifetime, the level of maximum net upward transport for the shallow but heavily precipitating clouds of Hawaii occurred at a level midway between cloud base and the base of the trade inversion at a height of roughly 1.3 km. Collapsing turrets that penetrated above the inversion produced net negative mass flux in the uppermost parts of the clouds. Near cloud base, convective updrafts early in the cloud lifetime were partially cancelled by downdrafts in decaying clouds.

A three-dimensional numerical simulation of an isolated trade cumulus cloud captured the dominant features of the evolution of the mass flux profile and suggested that precipitation has a weak effect on the vertical mass flux profile in the lifetime averages. The simulation produced larger mass fluxes near cloud base early in the cloud lifetime than were observed by the radar.

Our results differ markedly from mass flux profiles estimated from BOMEX and may not be representative of typical open-ocean nonprecipitating trade cumuli due to the larger population of deep clouds stimulated by lifting-induced destabilization of the HaRP boundary layer.

Typical conceptual models of cumulus clouds, such as the Raymond and Blyth (1992) buoyancy sorting model or entraining plume models, predict mass flux profiles similar to the early phase of our observations. However, the regions of negative mass flux characteristic of the mature and late phases are underestimated by these simple models.

Ultimately, a cumulus parameterization must be judged on its prediction of the vertical transport of heat, moisture, and momentum. A determination of the vertical mass flux profile in both updrafts and downdrafts

is one intermediate step in this process. We have focussed on this step because radar can observe the cumulus mass fluxes but not the area-averaged transport of heat, moisture, and momentum. This study and others underline the often-ignored role of downdrafts in shallow convective transports. With millimeter-wavelength radars, high-resolution LES models, and sophisticated cumulus parameterizations, the comparison between models and observations should be greatly tightened in upcoming years.

REFERENCES

Arakawa, A., and W. H. Schubert, 1974: Interaction of a cumulus cloud ensemble with the large-scale environment. Part I. *J. Atmos. Sci.,* **31,** 674–701.

Baker, M. B., 1993: Trade cumulus observations. *The Representation of Cumulus Convection in Numerical Models,* K. A. Emanuel and D. J. Raymond, Eds., *Meteor. Monogr.,* No. 46, Amer. Meteor. Soc., 17–28.

——, R. E. Breidenthal, T. W. Choularton, and J. Latham, 1984: The effects of turbulent mixing in clouds. *J. Atmos. Sci.,* **41,** 299–304.

Battan, L. J., 1973: *Radar Observation of the Atmosphere.* University of Chicago Press, 324 pp.

Baumgardner, D., and M. Spowart, 1990: Evaluation of the Forward Scattering Spectrometer Probe. Part III: Time response and laser inhomogeneity limitations. *J. Atmos. Oceanic Technol.,* **7,** 666–672.

——, W. Strapp, and J. E. Dye, 1985: Evaluation of the Forward Scattering Spectrometer Probe. Part II: Corrections for coincidence and dead-time losses. *J. Atmos. Oceanic Technol.,* **2,** 626–632.

Betts, A. K., 1973: A composite mesoscale cumulonimbus budget. *J. Atmos. Sci.,* **30,** 597–610.

——, 1975: Parametric interpretation of trade wind cumulus budget studies. *J. Atmos. Sci.,* **32,** 1934–1945.

——, 1985: Mixing line analysis of clouds and cloudy boundary layers. *J. Atmos. Sci.,* **42,** 2751–2763.

Braham, R. R., 1952: The water and energy budgets of the thunderstorm and their relation to thunderstorm development. *J. Meteor.,* **9,** 227–242.

Broadwell, J. E., and R. E. Breidenthal, 1982: A simple model of mixing and chemical reaction in a turbulent shear layer. *J. Fluid Mech.,* **125,** 397–410.

Byers, H. R., and E. C. Hull, 1949: Inflow patterns of thunderstorms as shown by winds aloft. *Bull. Amer. Meteor. Soc.,* **30,** 90–96.

Chen, C., and W. R. Cotton, 1987: The physics of the marine stratocumulus-capped mixed layer. *J. Atmos. Sci.,* **44,** 2951–2977.

Corrsin, S., 1951: On the spectrum of isotropic temperature fluctuations in an isotropic turbulence. *J. Appl. Phys.,* **22,** 469–473.

Doviak, R. J., and D. S. Zrnić, 1984: *Doppler Radar and Weather Observations.* Academic Press, 458 pp.

Dye, J. E., and D. Baumgardner, 1984: Evaluation of the Forward Scattering Spectrometer Probe. Part I: Electronic and optical studies. *J. Atmos. Oceanic Technol.,* **1,** 329–344.

Emanuel, K. A., 1991: A scheme for representing cumulus convection in large-scale models. *J. Atmos. Sci.,* **48,** 2313–2335.

Fankhauser, J. C., 1969: Convective processes resolved by a mesoscale rawinsonde network. *J. Appl. Meteor.,* **8,** 778–798.

——, 1974: The derivation of consistent fields of wind and geopotential height from mesoscale rawinsonde data. *J. Appl. Meteor.,* **13,** 637–646.

Frank, H. W., and G. B. Foote, 1982: The 22 July 1976 case study: Storm airflow, updraft structure, and mass flux from triple-Doppler measurements. *Hailstorms of the Central High Plains,* Vol. II, Colorado Associated University Press, 131–162.

Gossard, E. E., 1990: Radar research on the atmospheric boundary layer. *Radar in Meteorology,* D. Atlas, Ed., Amer. Meteor. Soc., 477–527.

——, and R. G. Strauch, 1983: *Radar Observations of Clear Air and Clouds.* Elsevier, 280 pp.

——, W. D. Neff, R. J. Zamora, and J. E. Gaynor, 1984: The fine structure of elevated refractive layers: Implications for over-the-horizon propagation and radar sounding systems. *Radio Sci.,* **19,** 1523–1533.

Houze, R. A., Jr., 1982: Cloud clusters and large-scale vertical motions in the tropics. *J. Meteor. Soc. Japan,* **60,** 396–409.

——, 1989: Observed structure of mesoscale convective systems and implications for large-scale heating. *Quart. J. Roy. Meteor. Soc.,* **115,** 425–461.

Joss, J., and A. Waldvogel, 1970: Raindrop size distributions and Doppler velocities. Preprints, *14th Radar Meteorology Conf.,* Boston, MA, Amer. Meteor. Soc., 153–156.

Knight, C. A., and L. J. Miller, 1993: First radar echoes from cumulus clouds. *Bull. Amer. Meteor. Soc.,* **74,** 179–188.

LeMone, M. A., and W. T. Pennell, 1976: The relationship of trade wind cumulus distribution to subcloud layer fluxes and structure. *Mon. Wea. Rev.,* **104,** 524–539.

——, and E. J. Zipser, 1980: Cumulonimbus vertical velocity events in GATE. Part I: Diameter, intensity, and mass flux. *J. Atmos. Sci.,* **37,** 2444–2457.

Leonard, B. P., M. K. MacVean, and A. P. Loch, 1993: Positivity preserving numerical schemes for multidimensional advection. NASA Tech. Memo. 1060555, ICOMP-93-05, 62 pp.

Lhermitte, R. M., 1970: Dual-Doppler radar observation of convective storm circulation. Preprints, *14th Radar Meteorology Conf.,* Boston, MA, Amer. Meteor. Soc., 139–144.

Mapes, B. E., and R. A. Houze Jr., 1993: Gregarious tropical convection. *J. Atmos. Sci.,* **50,** 2027–2037.

McNab, A. L., and A. K. Betts, 1978: A mesoscale budget study of cumulus convection. *Mon. Wea. Rev.,* **106,** 1317–1331.

Miller, L. J., F. I. Harris, and J. C. Fankhauser, 1982: The 22 June 1976 case study: Structure and evolution of internal airflow. *Hailstorms of the Central High Plains,* Vol. II, Colorado Associated University Press, 35–59.

Mohr, C. G., and R. L. Vaughn, 1979: An economical procedure for Cartesian interpolation and display of reflectivity factor in three-dimensional space. *J. Appl. Meteor.,* **18,** 661–670.

——, and L. J. Miller, 1983: CEDRIC—A software package for Cartesian space editing, synthesis and display of radar fields under interactive control. Preprints, *21st Conf. on Radar Meteor.,* Edmonton, AB, Canada, Amer. Meteorology Soc., 559–574.

Ogura, Y., and Phillips, N., 1962: Scale analysis of deep and shallow convection in the atmosphere. *J. Atmos. Sci.,* **19,** 173–179.

Ooyama, K., 1971: A theory on the parameterization of cumulus convection. *J. Meteor. Soc. Japan,* **49** (Special Issue), 744–756.

Ottersten, H., 1969: Radar backscattering from turbulent clear atmosphere. *Radio Sci.,* **4,** 1251–1255.

Paluch, I. R., 1979: The entrainment mechanism in Colorado cumuli. *J. Atmos. Sci.,* **36,** 2467–2478.

Raga, G., J. B. Jensen, and M. B. Baker, 1990: Characteristics of cumulus band clouds off the coast of Hawaii. *J. Atmos. Sci.,* **47,** 338–355.

Raymond, D. J., 1988: A C language-based modular system for analyzing and displaying gridded numerical data. *J. Atmos. Oceanic Technol.,* **5,** 501–511.

——, and M. Wilkening, 1985: Characteristics of mountain-induced thunderstorms and cumulus congestus clouds from budget studies. *J. Atmos. Sci.,* **42,** 773–783.

——, and A. M. Blyth, 1986: A stochastic mixing model for nonprecipitating cumulus clouds. *J. Atmos. Sci.,* **43,** 2708–2718.

——, and A. M. Blyth, 1992: Extension of the stochastic mixing model to cumulonimbus clouds. *J. Atmos. Sci.,* **49,** 1968–1983.

——, R. Solomon, and A. M. Blyth, 1991: Mass fluxes in New Mexico mountain thunderstorms from radar and aircraft measurements. *Quart. J. Roy. Meteor. Soc.,* **117,** 587–621.

Rogers, R. R., C. A. Knight, J. D. Tuttle, W. L. Ecklund, D. A. Carter, and S. A. Ethier, 1992: Radar reflectivity of clear air at wavelengths of 5.5 and 33 cm. *Radio Sci.,* **27,** 645–659.

Siebesma, A. P., and J. W. M. Cuijpers, 1995: Evaluation of parametric assumptions for shallow cumulus convection. *J. Atmos. Sci.,* **52,** 650–666.

Smolarkiewicz, P. K., and C. S. Bretherton, 1989: Gravity waves, compensating subsidence, and detrainment around cumulus clouds. *J. Atmos. Sci.,* **46,** 740–759.

——, and L. G. Margolin, 1993: On forward-in-time differencing for fluid: Extension to a curvilinear framework. *Mon. Wea. Rev.,* **121,** 1847–1859.

Sommeria, G., 1976: Three-dimensional simulation of turbulent processes in an undisturbed trade-wind boundary layer. *J. Atmos. Sci.,* **33,** 216–241.

Stevens, D. E., 1994: An adaptive multilevel method for boundary layer meteorology. Ph.D. dissertation, University of Washington, 105 pp.

Stommel, H., 1947: Entrainment of air into a cumulus cloud. *J. Meteor.,* **4,** 91–94.

Takahashi, T., K. Yoneyama, and Y. Tsubota, 1989: Rain duration in Hawaiian trade-wind rainbands—Aircraft observations. *J. Atmos. Sci.,* **46,** 937–955.

Tatarski, V. I., 1961: *Wave Propagation in a Turbulent Medium.* McGraw-Hill, 285 pp.

Telford, J. W., and P. B. Wagner, 1974: The measurement of horizontal air motion near clouds from aircraft. *J. Atmos. Sci.,* **31,** 2066–2080.

Tiedtke, M., W. A. Heckley, and J. Slingo, 1988: Tropical forecasting at ECMWF: The influence of physical parameterization on the mean structure of forecasts and analyses. *Quart. J. Roy. Meteor. Soc.,* **114,** 639–664.

Yuter, S. E., and R. A. Houze Jr., 1995: Three-dimensional kinematic and microphysical evolution of Florida cumulonimbus. Part III: Vertical mass transport, mass divergence, and synthesis. *Mon. Wea. Rev.,* **123,** 1964–1983.

Zalesak, S. T., 1979: Fully multidimensional flux-corrected transport algorithms for fluids. *J. Comp. Phys.,* **31,** 335–363.